Neuronal pattern separation in the olfactory bulb improves odor discrimination learning

Olivier Gschwend[#1,2], **Nixon M. Abraham**[#1,2,3], **Samuel Lagier**[1,2], **Frédéric Begnaud**[4], **Ivan Rodriguez**[2,3], and **Alan Carleton**[1,2]

[1]Department of Basic Neurosciences, School of Medicine, University of Geneva, 1 rue Michel-Servet, 1211 Geneva 4, Switzerland [2]Geneva Neuroscience Center, University of Geneva, Switzerland [3]Department of Genetics and Evolution, University of Geneva, 1211 Geneva, Switzerland [4]Firmenich SA, Corporate R&D Division / Analytical Innovation, route des Jeunes 1, CH-1211 Geneva 8, Switzerland

[#] These authors contributed equally to this work.

Abstract

Neuronal pattern separation is thought to enable the brain to disambiguate sensory stimuli with overlapping features thereby extracting valuable information. In the olfactory system, it remains unknown whether pattern separation acts as a driving force for sensory discrimination and the learning thereof. Here we show that overlapping odor-evoked input patterns to the mouse olfactory bulb (OB) are dynamically reformatted in the network at the timescale of a single breath, giving rise to separated patterns of activity in ensemble of output neurons (mitral/tufted cells; M/T). Strikingly, the extent of pattern separation in M/T assemblies predicts behavioral discrimination performance during the learning phase. Furthermore, exciting or inhibiting GABAergic OB interneurons, using optogenetics or pharmacogenetics, altered pattern separation and thereby odor discrimination learning in a bidirectional way. In conclusion, we propose that the OB network can act as a pattern separator facilitating olfactory stimuli distinction, a process that is sculpted by synaptic inhibition.

Keywords

Introduction

The optimal disambiguation of overlapping sensory stimuli by neuronal networks is an essential process to build internal representations of the external world. Along sensory pathways, precortical[1—5] and cortical[5—8] networks have been proposed to drive this disambiguation through pattern separation, also known as pattern decorrelation[9,10]. This process is thought to increase the formation of discrete representations and is considered to be useful for discrimination and memory storage[9—11]. Despite these observations, the timescales and the behavioral relevance of pattern separation remain elusive.

In the rodent OB, odorants evoke discrete spatiotemporal patterns of activated glomeruli in awake mice[12,13]. The spatial segregation helps separating channels of information and thereby increasing contrast between odor-evoked activities. However, similar stimuli such as binary mixtures evoke overlapping representations of activated glomeruli[14—17]. Yet, these odorant stimuli are still discriminable by animals[14,18—20], indicating that overlapping sensory information is further refined along the sensory pathway as observed in the piriform cortex (PC)[5,21,22]. In the zebrafish OB, this refinement, namely pattern separation, acts to reduce overlapping odorant-evoked activity patterns in the population of output neurons (mitral/tufted cells, M/T)[1,2,23]. But the existence of a similar process in the mammalian olfactory system has not been clearly established. More importantly, the behavioral relevance of pattern separation is still debated[24] and thus far no studies have addressed this question. Therefore it remains unknown whether pattern separation is a driving force for sensory discrimination and the learning thereof.

Here we show, using functional imaging, tetrode recordings, optogenetic and pharmacogenetic manipulations in awake mice, that pattern separation in the OB plays an important role in olfactory discrimination learning. Similar odorant stimuli evoked overlapping input patterns of olfactory sensory neuron (OSN) axons that were dynamically reformatted in ensembles of OB output neurons (mitral/tufted cells; M/T) at the timescale of a single sniff, helping the separation of such overlapping inputs. Strikingly, the extent of pattern separation in the OB predicted the mice' ability to discriminate olfactory stimuli during the early learning phase. To further investigate the causality between pattern separation and discrimination performance, odor-evoked M/T cells responses were modulated by enhancing or suppressing inhibitory interneuron activity in the granule cell layer (GCL) using channelrhodopsin (ChR2) photostimulation or a designer receptor exclusively activated by designer drugs (hM4Di Gi-DREADD), respectively. Enhancing inhibition of M/T cells increased odor-evoked output pattern separation and improved odor discrimination learning. In contrast, silencing GCL neurons with Gi-DREADD caused a decrease of pattern separation and a deterioration of odor discrimination learning. In conclusion, our data indicate that the OB network acts as a pattern separator to facilitate olfactory stimuli discriminations, a process that can be controlled by OB GABAergic neurons.

RESULTS

Similar odors evoke correlated input patterns to the OB

To test how efficiently the olfactory system may separate similar odor-evoked representations, we aimed at generating a large set of odorant stimuli evoking input patterns that vary in similarity. We investigated the complex representation of OB sensory inputs by imaging odor-evoked Ca^{2+} responses in the glomerular layer of awake head-restrained transgenic mice expressing the genetically encoded calcium indicator GCaMP3 in olfactory sensory neurons[13] (OSNs, Fig. 1a and Supplementary Fig. 1). We used two groups of binary mixtures – amyl acetate/ethyl butyrate (AA/EB) and ethyl butyrate/3-hexanone (EB/HX) – composed of variable relative ratios of individual components mixed either in gaseous or liquid phases. The gaseous and liquid mixtures having the same presumed ratios differed consistently and could be attributed to the chemical properties of resulting mixtures such as relative composition and total concentration. This was highlighted by the analytical studies of binary mixtures using gas chromatography combined to flame ionization detection (GC-FID, see methods and Supplementary Table 1; total FID area concentrations ranged from ~1000 to 10000). Nevertheless, related mixtures evoked similar spatiotemporal patterns of glomerular activity (Fig. 1a,b). To quantify the similarity, we combined the fluorescence change of activated glomeruli in a population vector binned over an entire breath and further computed the Pearson correlation coefficient between vectors of activity evoked by each mixture, either for each mouse or for all animals (yielding similar results; Fig. 1c,d and Supplementary Fig. 1). The systematic comparison of all possible mixtures to each other was reported in a correlation matrix which revealed that binary mixtures with identical components at different ratios (either AA/EB or EB/HX mixtures) evoked highly correlated patterns of activity, whereas binary mixtures with different components (AA/EB vs. EB/HX mixtures) evoked less correlated patterns (Fig. 1c-e and Supplementary Fig. 1f). This observation was consistent throughout the time course of the first breath following odor presentation onset (Fig. 1e-f and Supplementary Fig. 1g).

Importantly, input correlation was not correlated to the amplitude of glomerular responses (Supplementary Fig. 2). Moreover, the odorant concentration used is the study did not saturate OSN response (Supplementary Fig. 3). Finally, input correlation across mixtures was similar for weakly and strongly activated glomeruli (Supplementary Fig. 4), indicating that strong glomerular responses do not impose the level of input correlation. The differences between input representations are therefore neither due to saturation of the calcium dye nor due to strongly and potentially saturating OSN responses, which may have both compressed the dynamic range of the calcium imaging readout.

Taken together, these data suggest that binary mixtures sharing the same pre-determined component ratios evoke highly correlated input patterns to the OB, irrespective of the subtle differences caused by gaseous and liquid phase mixing.

OB reformatting of odor representations in a single breath

Despite similarities between odorant-evoked input patterns, trained rodents can discriminate monomolecular odorants or mixtures in less than 400 ms, which corresponds to the duration

of one or two breaths[14,18—20,25—27]. The olfactory bulb network may thus process sensory inputs in order to separate overlapping information. To test this assumption, single M/T cell units ($n = 377$ cells from 18 mice) were recorded in the OB of awake head-restrained mice while presenting various odorants[13,28,29] (Fig. 2a). Neurons displayed complex responses to odorants such as phasic, tonic, excitatory, inhibitory or bimodal ($n = 1248$ odor-cell pairs in 6 mice, Fig. 2b-e and $n = 1859$ and 1430 odor-cell pairs in 4 and 8 mice, respectively, Supplementary Fig. 5a-d; different datasets were used to ascertain the reproducibility of population correlation in different animal groups). In order to compare the similarity of output patterns evoked by different mixtures, we computed the Pearson correlation between population vectors of M/T cell activity averaged over the first breath duration after odor onset evoked by different mixtures. Notably, the output correlation matrix differed from the one computed at the input level, suggesting that sensory representations are indeed reformatted within the OB synaptic pathway (compare Fig. 2f,g to Fig. 1c,d). Some groups of mixtures that were correlated at the input level became decorrelated at the output level whereas others remained unchanged (compare Fig. 2g to Fig. 1d). Though there was an overall reduction of output correlation, few mixtures evoked more correlated patterns at the output level than at the input level (points above the diagonal in Fig. 2h), suggesting a non-linear reduction of input to output correlations over all odors.

We then analyzed the output correlation at a finer time scale. Interestingly, the level of correlation between output patterns significantly evolved over the time course of the first and subsequent breaths, groups of mixtures becoming significantly decorrelated over time (Fig. 3a,b, Supplementary Fig. 5e-h and Supplementary Fig. 6). For some mixtures, decorrelation was rapid (e.g. red and blue curves in Fig. 3b,c and Supplementary Fig. 5e,f), which is consistent with some mitral cells responding to the early glomerular response (i.e. first 80ms in Fig. 1e,f). In contrast, correlation was increasing in the first 120 ms and then decreasing in the remaining part of the breath for other mixtures (e.g. cyan and magenta curves in Fig. 3b,c and Supplementary Fig. 5g,h), which likely relates to the increase of input correlation seen in Fig. 1f. Nevertheless, a significant decorrelation was observed for all subgroups of mixtures during the first breath (Fig. 3c). A similar decorrelation was observed after subtracting baseline firing activity (Fig. 3d,e), indicating that the process is independent from sniff-related baseline dynamics and from non-responding cells. Since input correlation reached a maximum around 120 ms, we further analyzed the output correlation from this time point of the first breath. We observed a significant decorrelation process taking place between 126 and 252 ms (Fig. 3e). Furthermore, increasing the temporal resolution by averaging mitral/tufted firing over a 21 ms time window revealed that output patterns were significantly decorrelated in ~80—100 ms after the peak of input correlation (Fig. 3f and Supplementary Fig. 7a).

Interestingly differences in the population firing rate evoked by different mixtures could not explain the observed correlation differences (Fig. 4). Furthermore the extent and dynamics of pattern correlation for different groups of mixtures depended neither on cell sampling nor on single cell response property since similar correlation behavior was observed for independently recorded datasets for which neurons displayed dissimilar response profiles (compare Figs. 2,3 and Supplementary Fig. 5). The main differences of correlation observed for different mixtures might instead be due to the variation of component concentration and

absolute number of molecules in the mixtures, as reported by our GC-FID analysis (Supplementary Table 1 and see methods). Taken together, these results suggest that a reformatting of activity occurs in the OB, which tends to increase the separation of representations evoked by similar mixtures over a breathing cycle.

Output pattern similarity predicts learning performances

Does pattern separation taking place over the time course of a breath help animals to discriminate related odorants in a behavioral task? To address this question, we trained mice on a head-restrained go/no-go operant discrimination paradigm[19] and tested eleven pairs of odorants that we selected based on the amount of output correlation they elicited (Fig. 5a,b). While the extent of input correlation over the first post-odor breath was not a good predictor of discrimination performances, we observed in contrast a significant correlation between M/T ensemble correlation and discrimination performances during the initial learning phase, defined here as the average of the first 300 trials (Fig. 5c—e). Similar results were observed when considering the mean and the minimum of the output correlation (Fig. 5d,e) or when output correlation was quantified only after the maximum of input correlation had been reached (Supplementary Fig. 7b—e). These data suggest that the extent of pattern separation in the OB predicts the ability of mice to discriminate between two odorants: the more the patterns are separated; the faster the odor discrimination learning takes place.

GABA neurons modulate pattern separation and learning

To further test the causal relationship between pattern separation and odor discriminability, we aimed to manipulate the OB outputs using optogenetics. Theoretical works suggest that pattern decorrelation may depend on OB inhibitory interneurons[23,30—32]. Therefore, we expressed channelrhodopsin2-YFP (ChR2) in interneurons of the granule cell layer using adeno-associated viral (AAV) vectors[18] (Fig 6a,b). Immunohistochemical analysis of the infected brains revealed an infection exclusively restricted to the GCL in which ~35% of the neurons were transfected (Supplementary Fig. 8). We further performed extracellular recordings of M/T cells using optrodes ($n = 38$ cells from 6 mice; Fig 6c,d). Photostimulation significantly inhibited 38% of the total odor-M/T cell pairs ($n = 228$, χ^2 test, $P = 0.01$). Light-evoked inhibition was cell-specific and M/T cell responses evoked by each odorant were not linearly inhibited (Fig. 6e,f). Together, these results suggest that the photostimulation triggered a specific modulation of tuning properties rather than an unspecific gain control. Though the average population rate was significantly reduced by light stimulation either during air or odor presentation (Fig. 6g), photostimulation enhanced pattern decorrelation over the breath time course only during the odor epoch for mixtures (Fig. 6h). The light-induced decorrelation was visible across the breathing cycle (Fig. 6i). In summary, photoactivation of inhibitory neurons in the GC layer modulates individual M/T cells activity and promotes pattern decorrelation.

Considering our observations that the extent of pattern separation correlates with odor-discrimination learning (Fig. 5), one would expect that enhancement of decorrelation should improve odor-discrimination performance. To test this hypothesis, we trained two cohorts of mice (expressing either enhanced green fluorescence protein [EGFP] or ChR2-YFP in neurons of the granule cell layer) on different mixture discrimination tasks. Head-restrained

mice were photostimulated using a LED implanted on a cranial window overlaying both olfactory bulbs (Fig. 6j, Supplementary Fig. 9a,b and see methods). At high light power, animals strongly reduced their licking behavior in an olfactory association task (Supplementary Fig. 9c,d), suggesting a global silencing of M/T cells. In order to avoid such effect, we gradually reduced the light power until complete recovery of the normal licking behavior. This optimized power was then used during odor discrimination tasks. ChR2-expressing mice learned mixture discriminations faster than control mice but reached similar final performance levels (AA/EB and EB/HX mixtures in Fig. 6k). This effect was specific to photostimulation since the discrimination performance evolved similarly in both cohorts when two other mixtures were subsequently tested in the absence of light stimulation (C+/C − and AC/LI mixtures in Fig. 6k). Then, in order to reconfirm the photostimulation effect, we trained the same mice on yet another binary mixture pair. Again, light stimulation significantly enhanced learning performances without altering the final performance levels in the ChR2-expressing mice (HO/HA mixtures in Fig. 6k).

We next questioned whether stimulating GCL neurons would have similar impact on simple odor discrimination tasks. Interestingly M/T cell correlation for the monomolecular compounds present in the mixtures was not affected by ChR2 stimulation (Supplementary Fig.10a). Consistent with the electrophysiology, ChR2 stimulation did not affect the learning pace for simple odor discrimination task in an additional cohort of mice (Supplementary Fig. 10b). In contrast, but consistent with our first cohort, learning pace for difficult discrimination tasks (mixtures) was improved by photostimulation of GCL neurons (Supplementary Fig. 10c). Likewise, photostimulation specifically enhanced reaction times for difficult discrimination tasks (Supplementary Fig. 10d). These results confirm that pattern separation is a process mainly required to disambiguate overlapping OSN inputs representation.

We finally tested whether inhibiting GCL neurons would have an opposite effect on pattern separation and odor discrimination learning. We thus tested the effect of silencing the GCL population using inhibitory pharmacogenetic manipulation (hM4Di Gi-DREADD cohort). We recorded odor-evoked responses of M/T cells before and after DREADD activation by clozapine-N-oxide (CNO) injection. CNO injection increased odor-evoked firing rates in DREADD infected mice but not in ChR2 expressing mice (used as controls, Fig. 7a,b), leading to a specific increase of ensemble correlation in DREADD mice (Fig. 7c). We finally tested whether such decrease in pattern separation would affect odor discrimination. As predicted, silencing granule cell layer neurons using pharmacogenetics decreased odorant discrimination learning pace for complex odors (Fig. 7d).

In conclusion, these results demonstrate that bidirectional manipulation of GABAergic neurons of the GCL modulates the decorrelation of overlapping M/T cell activity patterns, which controls the ability of animals to learn to discriminate between similar odorants.

DISCUSSION

Our work provides evidence that overlapping glomerular maps evoked by related odorants can be separated by the OB network (up to certain level of similarity). This neural

reformatting, which occurs during a single sniff, helps to disambiguate similar odorants and improves odorant discrimination learning. Finally, pattern separation can be promoted by the interplay between M/T cells and GABAergic neurons.

Overlapping OSN inputs can be decorrelated into separated patterns of M/T cell activity in a single breath (Figs. 1-3). Though we observed an overall decrease of correlation between input and output patterns, some mixtures evoked output patterns that remained highly correlated or even exhibited an increase of correlation compared to input patterns (Fig. 2). We do not think that the input/output transformation can simply be explained by the use of different recording techniques. Indeed, though the differences in sensitivity and temporal resolution between the two techniques may limit the direct comparison of correlation at 40 ms time scale, such limitations are no longer valid when the patterns of activity are averaged and compared over the complete breath duration. Furthermore, higher correlation observed at the input level for some mixtures cannot be explained by overestimated correlation resulting from possible calcium dye saturation for strongly activated glomeruli (Supplementary Figs. 2―4). In conclusion, odorant stimuli undergo an input/output reformatting in the OB involving a nonlinear reduction of correlation.

While in the past several groups have analyzed coding properties in the rodent olfactory bulb, the existence of pattern separation was often eluded, probably because of the use of a limited number of related odorant stimuli or the absence of neuronal population analyses. Yet, some authors questioned the role of OB (in comparison to the PC) to compute pattern separation using odor blends[4,5]. They reported a drop of correlation when comparing across-trials correlation vs. across-mixtures correlation, which in fact does not correspond to a pattern separation process. In addition, they did not observe any significant decorrelation between similar mixtures. In contrast, here we show that decorrelation of similar mixtures occurred in the OB with temporal dynamics that varied for different subgroups of mixtures (Fig. 3 and Supplementary Fig. 5), probably reflecting temporal patterning of M/T cell spiking[13,25,28,33]. Strikingly, decorrelation occurs in 80-100 ms after the peak of input correlation within the first breath after odor onset, providing a relevant timescale for the reaction time measured during olfactory-driven behaviors[14,25―27] (Supplementary Fig. 10).

In both insects and vertebrates, the anatomical segregation of glomeruli constitutes the first step to differentiate channels of information and help animals to discriminate between odorants. Though discrimination behavior can be predicted to some extent by the similarity of glomerular responses[14,34,35], this prediction is not efficient at the early learning phase of novel odorants[14]. Here using a large set of mixtures varying in similarity, we could confirm that glomerular input correlation is not a good predictor of discrimination learning for novel odorants (Fig. 5). In contrast, initial behavioral performances were clearly predicted by the output correlation during the complete breath (Fig. 5). Interestingly, the fast decorrelation process taking place following the peak of input correlation also significantly predicts behavioral performances (Supplementary Fig. 7). These results support the idea that overlapping activity patterns are separated at the level of the OB network. Importantly, optogenetic and pharmacogenetic manipulations of the OB network further support this view (Figs 6 and 7). It is noteworthy that learning performances for simple odorants were not affected by optogenetic manipulations in contrast to the learning of mixtures

(Supplementary Fig. 10). In conclusion, while very different glomerular patterns would not require further separation in the OB network, as observed in the case of monomolecular odorants (Supplementary Fig. 10), our results emphasize the functional relevance of OB-mediated pattern separation in processing similar odorants.

In summary, as it has been hypothesized by experimental[1,36,37] and modelling studies[23] for a long time but never demonstrated, our work provide evidence for a functional role of pattern separation at a pre-cortical level.

Using optogenetic and pharmacogenetic manipulations, we provide evidence that the interplay between M/T cells and GCL neurons affects pattern separation (Figs. 6 and 7). Interestingly, the odor specificity of evoked inputs matters since ChR2-mediated GC recruitment does not linearly reduce the tuning curve of M/T cells but rather changes its shape (Fig. 6). These data suggest that GC layer photostimulation preferentially changes the odor selectivity rather than the gain, in contrast to other GABAergic interneurons such as such as parvalbumin cells of the external plexiform layer[38,39].

Consistent with our observations, computational and *in vitro* works speculated that GC-dependent gating of M/T cells should enhance channel decorrelation, reduce spiking similarities between pairs of M/T cells and further improve pattern separation[30,31]. Supported by recent *in vivo* work, other models speculated in contrast that periglomerular cells (PG) may reduce similarity between odor-evoked M/T cells representations through non-topographical contrast enhancement[40]. GC would hence preferentially modulate fast gamma oscillations without substantial change of M/T cells firing rate[41]. However, our optogenetic and pharmacogenetic manipulations of GCL neurons contrasts with this idea, showing that those neurons can in fact enhance contrast between related odorants. As channel decorrelation or non-topographical contrast enhancement can occur separately from pattern separation[42], it is possible that they constitute different or complementary processes[10]. Nevertheless, future work will be needed to test the possible contribution of other subpopulations of OB interneurons[38,43], adult-born interneurons[44,45] or other mechanisms such as intrinsic biophysical properties[46] of M/T cells to pattern separation.

How the GC to M/T cell inhibition is recruited is critical for the control of olfactory discrimination behavior. Indeed, the deletion of the AMPA receptor subunit GluA2 in GCs, while boosting synaptic Ca^{2+} influx and thus M/T cell dendrodendritic inhibition, does not change odor discrimination learning pace[18]. In the present work, ChR2-GC layer photostimulation may force a more global, but still specific, GABA release mimicking an increase of synaptic weight[23], favoring pattern decorrelation and improving the learning pace. The ChR2 condition might relate to M/T cells inhibition induced by cortical feedback projections onto granule cells[47,48].

What is the relevance of pattern separation for downstream networks? In the recorded neuronal population, pattern separation is mainly processed by M/T cells responding with temporal changes of firing (Fig. 2 and Supplementary Fig. 5), possibly enhancing fine temporal differences between overlapping odor-evoked patterns. As the PC is able to

integrate temporally shifted OB outputs[49], pattern separation may broaden the range of PC neurons that are sensitive to different temporal integration windows.

While our data showed that pattern separation occurs in the OB, a previous work indicates that this process occurs downstream, in the PC[5]. It is possible that, after an extensive training, the PC separates patterns of activity evoked by similar stimuli that the OB fails to segregate[5]. Alternatively, the PC may preferentially process pattern completion[5]. Indeed, the PC, like the hippocampus, is an auto associative area, which is thought to process pattern storage and recall[11,50]. The OB and the dentate gyrus may comparably reduce correlated inputs to the PC and CA3 respectively in order to prevent misclassification of patterns and facilitate memory formation.

In conclusion, pattern separation might constitute an efficient network feature shared by different brain structures to properly identify stimuli eliciting a combinatorial of overlapping inputs and thereby promoting better discrimination.

ONLINE METHODS

Animals and initial preparation

Behavior and electrophysiology experiments were performed at the beginning of experiments on 8 to 16 week-old male C57BL/6J mice (Janvier, France). Imaging was done on 8 week-old Omp[cre/+]Rosa[flox-stop-flox-GCaMP3/+] male mice (i.e. Omp[tm4(cre)Mom 51]; JAX 006668 and Gt(ROSA)26Sortm38(CAG-GCaMP3)Hze/J [52]; JAX 014538, respectively). None of the experiments were blind of the genotype. Mice were housed in groups of 3―5 in a state of the art animal facility (12hours light/dark cycles). All experiments were done during daytime. All experiments were done in accordance with the Swiss Federal Act on Animal Protection and Swiss Animal Protection Ordinance. Experiments were approved by the University of Geneva and the Geneva state ethics committees (authorizations 1007/3387/2 and GE/156/14).

Mice were anesthetized with isofluorane (3―4 % induction, 1―2% maintenance). The skin overlaying the skull was removed under local anaesthesia using carbostesin (AstraZeneca, Zug, Switzerland). A steel head-post was then fixed on the bone by embedding its base in dental cement (Omni-Etch Dentin, OmniDent). The rest of the skull was also covered with dental cement except the part overlaying the OB. Animals were then put back to their cage and allowed to recover for couple of days.

Few days after recovery, mice were trained to be head-restrained. They were placed in a plastic tube and head-fixed by screwing the head-post on a custom-made holder fixed on the air table (Fig. 2a). Mice were trained to this restraining condition for 2―4 sessions (30―60 min each) done in 2―3 days.

Odor delivery and experimental protocol

All odorants (amyl acetate: AA, ethyl butyrate: EB, 3-hexanone: HX, carvone +: C+, carvone −: C−, acetophenone: AC, limonene: LI, heptanal: HA, hexanol: HO) were from Sigma-Aldrich. We used the following mixtures: AA/EB 80%/20%, 60%/40%, 40%/60%,

20%/80%, EB/HX 80%/20%, 60%/40%, 40%/60%, 20%/80% but also simple component in some case such as AA/air 60%/40%, EB/air 60%/40% and HX/air 60%/40%.

4 mL of pure odorant or mixtures of odorants were placed in glass vials. Binary mixtures were made by mixing the odorant plumes in gaseous phase or by directly mixing in liquid phase. Varying the relative flow of independent stream of odorized air allowed mixing of odors in gaseous phase. Unexpectedly, the way mixtures were prepared had an impact on the electrophysiology and behavioral read-outs (see next section).

Odorants were delivered for 1.5—2 seconds through a custom made olfactometer as described previously[13,28,33,53]. The odorant onset was set at the end of an inspiration. Airflow passed through the vials containing the odorants and was further diluted 20 times with clean dry air before being sent to the nose. The total flow was constant (400 sccm, Standard Cubic Centimeter per Minute). To maintain a stable odor concentration during the entire stimulus application, we ensured that flows were stationary with a 3 s preloading before the odorant was delivered to the animal.

Measurement of ratios and concentrations in mixtures

We found in this study that the way mixtures were prepared had a strong impact on the electrophysiology and behavioral read-outs. The purpose of this study is not to explain the physico-chemical parameters leading to such difference. However, to gain more insight into the possible difference in composition of various mixtures, we estimated the composition of different mixtures using gas chromatography-flame ionization detector system (GC-FID). We observed that the various mixtures were indeed different. We report the quantification done with the GC-FID which measures two parameters: the relative ratio between two components and the mass of compounds reaching the detector that we can relate to the total amount of molecules (Supplementary Table 1). Since we could not sort the correlation profile based on only one of these parameters, we decided to keep the mixing procedure with theoretical values, which also preserved coherent groups of correlated mixtures. Most likely, the combination of monomolecular components identity, relative ratio and total amount of molecules (i.e. concentration) is determining the neural responses and correlation behaviors, but further experiments are needed to clarify which physico-chemical parameter is critical in forming the percepts.

The GC-FID analysis involved two steps:

1.   Collection of binary mixture vapors from the output of olfactometer using NeedlEx

NeedlEx is a luer lock needle with side hole: inner diameter 0.5 mm, outer diameter 0.7 mm and length 85 mm (Shinwa Chemical Industries Ltd, Japan). We used the NeedlEx specific for organic solvents, which is packed with a layer of a polymer material (a copolymer of methacrylic acid and ethylene glycol dimethacrylate). Prior to odorant collection, the NeedlEx was conditioned at 200 °C in a gas chromatograph injection port (set to 100 kPa of Helium with a 200:1 split) for 1 hour before the very first usage of NeedlEx and for 5 minutes before each sample collection by

keeping the top of the needle open to eliminate all possible contaminants. The NeedlEx was protected from contamination by closing both ends using Teflon caps when not in use. After conditioning, samples from the olfactometer gas flow were collected by actively pumping 50mL of gas through the Needlex using a calibrated pump.

2.   Analysis of binary mixtures using GC-FID

Sixty samples corresponding to 2s odor presentation were cumulatively trapped by Needlex to get a consistent readout from GC-FID analysis. Immediately after sampling, the Needlex was transferred to the hot injection port of the GC for desorbing the compounds. Desorption time was set to 3 minutes. The desorbed vapors were then analyzed by the FID connected to the GC. In order to get robust values, we repeated the experiment 5—8 times for each mixture. The amount of molecules was quantified using the area of the GC-FID peak corrected by their relative response factor relative to EB. Response factors relative to EB have been determined by injecting mixtures of EB and AA or EB and HX at pre-determined concentration in the GC-FID.

Flame ionization detector (FID) is a robust and highly linear mass dependent detector widely used in gas chromatography. Its response is strongly correlated to the number of carbon atoms of organic molecules and the corresponding mass to peak area proportionality coefficient is called response factor (RF). However, RF is notably influenced by heteroatoms[54] and can vary substantially between molecules. Consequently, considering two molecules, their FID peak area ratio may not reflect accurately their mass ratio. To correct for this difference of RF, one can inject a concentration-controlled mixture of a standard together with a molecule of interest. It is known that the ratio of peak area and the ratio of mass of compound and standard are proportional. The proportionality coefficient corresponds to the ratio of RF and is called the Relative Response Factor (RRF). Applying these RRFs to all studied molecules led to accurate relative mass comparisons. In our study, we considered one of the three compounds to be the standard (EB) since it was a shared component of all mixtures.

$$\text{Response factor relative to } EB \text{ for compound } X = \frac{\text{Area } EB}{\text{Area } X} * \frac{\text{mass } X}{\text{mass } EB}$$

The actual amount of molecules has not been determined. The percentage of each component in a binary mixture, for example AA-EB mixture, was calculated as following:

$$\%AA = \frac{AA \text{ peak area} * \text{Response factor relative to } EB}{(AA \text{ peak area} * \text{Response factor relative to } EB + EB \text{ peak area})} * 100$$

After correction using response factors ($RRF_{HX} = 0.777$ and $RRF_{AA} = 0.854$), the total intensity of the stimuli was calculated by summing the corrected FID areas corresponding to the individual components.

In vivo imaging

On the day of the imaging session, animals were anesthetized with isoflurane and the skin atop the olfactory bulb was removed after a topical injection of carbostesin. The skull was thinned to allow optimal optical access to the left OB. Imaging started after at least a 30 min recovery period following the end of anesthesia. Images were acquired at 25Hz using the Micam Ultima system (Brainvision, Tokyo, Japan) mounted on a custom build microscope (Navitar 17 mm, bottom lens, Nikon 135mm, upper lens; total magnification 7.9×)[12,13]. Pixel values of collected images were computed as F/F. All odorants were presented 10 times in a pseudo-randomized order. The first trial was discarded from the analysis due to fast sniffing causing motion artefacts in the images. For all experiments, respiration was monitored using a bidirectional air flow sensor (AWM2100V, Honeywell, MN) placed in front of the mouse nose. The device, though close to one nostril, did not prevent the odorant to reach the other nostril (connected to the recorded OB).

For analysis, absolute F/F values were analyzed as a proxy for neural activity in OSN terminals. Analysis have been performed either on manually selected regions of interest (ROI) or on all pixels covering the OB surface, giving similar results (Supplementary Fig. 1). For the ROI analysis, ovoid regions displaying sustained increase in fluorescence during consecutive breaths following odorant application were manually delineated. All ROI activated by at least one mixture (at least 30 ROI per animal, $n = 4$ animals) were included in the analysis. To calculate the correlation between odorant-evoked patterns of glomeruli, change in fluorescence was calculated for each ROI either over the first breath after odorant application or in consecutive 40ms time windows during the first breath (Fig. 1c―e). Vectors of ROI activity were generated for each mixture and used to calculate correlations and further create correlation matrices. The correlations were computed either on single animal (correlation matrices being then averaged across animals, Fig. 1c―e, Supplementary Fig. 1a―d) or by concatenating all ROI coming from different mice (Supplementary Fig. 1e―g), giving similar results. For the pixel analysis, in each animal, after realigning all image series acquired for different mixtures using the resting fluorescence, a ROI encompassing the entire dorsal olfactory bulb was drawn. All individual pixels in the ROI were used to calculate correlation between patterns of activity evoked by different mixtures as mentioned above for the ROI analysis.

In vivo electrophysiological recordings and spike sorting

On the day of the experiment, mice were head-restrained and anesthetized with isoflurane (3% induction, 0.75―1% maintenance). A 1―2mm window was made by drilling the skull above the olfactory bulb and a silicon-based recording electrode (A―4×2―Tet―5mm―150―200―312, NeuroNexus Technologies, Ann Arbor, MI, USA) was inserted (Fig. 2a). The skull cavity was filled with an ophthalmic gel (Lacryvisc, Alcon) to protect the brain from drying. A silver wire contacting the gel was connected to the air table to ground the preparation. Electrodes were lowered in the target zone until reaching the medial mitral/tufted cell layer (MCL). We waited for the complete recovery of animals from anaesthesia. This period lasted for around 45―60 minutes, which also allowed the tissue to recover from electrodes penetration. For all experiments, respiration was monitored using a

bidirectional air flow sensor (AWM2100V, Honeywell, MN) placed in front of the mouse nose.

For the recording during optogenetic manipulation, we used a 32 channels optrode (Neuronexus technology, A1×32—Poly3—OA32; Fig. 6). We chose three binary mixtures (all mixing done in gaseous phase), AA/EB 60/40 and 40/60, EB/HX 60/40 and 40/60 and hexanol/heptanal (HO/HA) 60/40 and 40/60. Before each experiment, the power was set to ~1—30mW with a photodiode sensor (Thorlabs, Germany) coupled to a power meter (PM100D, Thorlabs) and measured at end of a 200 μm fiber optic going out from the 473nm laser driver (Shanghai Dream Laser; SDL—473–050MFL; China). We set the maximum light intensity that shut down the M/T cells baseline activity. We then gradually reduced the light power until recovering partially the spike rate. As the inhibitory effect varied depending on the electrode location and ChR2 expression, power varied from 24 to 95 mW/mm^2 (integrated power for 2s at the tip of the 105 μm diameter fiber glued on the optrode). Light activation was triggered with the odorant onset that is to say at end of an expiration. During odor presentation, transfected neurons of the GCL were photostimulated with eighty 5 ms-long pulses at 40 Hz [44]. This stimulation ranges in the gamma band and is optimal to drive GCs[30,55,56].

For the DREADD positive mice, we used the same odors as for the ChR2 positive mice. 10 trials of the different stimuli were presented pseudorandomly before CNO injection. After these trials, CNO was injected (2 mg/kg) 15—30 min before launching the next trials. After this period, 10 trials of the different stimuli were again applied pseudorandomly. CNO was injected either IP after anesthetizing shortly the mouse with isofluorane or either sub-cutaneous using a homemade cannula fixed on the skin using superglue. In the latter case, CNO was injected while the mouse was awake. We used the exact same procedure for the ChR2 positive mice that we used as a control for the DREADD positive mice.

Further details about recording and spike sorting have been described extensively elsewhere[13,28,33]. In brief, wide-band field potentials were amplified (100×) and band-pass filtered (0.1 Hz to 9 kHz). All data was digitized at 32556 Hz with the Cheetah Digital Lynx system (Neuralynx, Tucson, AZ). Spikes were detected by a threshold on the high-pass filtered signal, decomposed in 16 features, and automatically clustered. Individual neurons were finally identified if the clusters showed a clean refractory period in their autocorrelograms. 78 neurons from 6 mice were isolated for dataset 1 (Supplementary table 2). 169 isolated neurons were isolated from 4 mice for dataset 2. 130 were isolated from 8 mice for dataset 3. 38 cells were recorded from 6 ChR2 positive mice (dataset 4). 55 cells were recorded from 5 DREADD positive mice (dataset 5). 40 cells were recorded from the ChR2-positive mice that were used as a control for the DREADD mice (dataset 6). 39 cells were recorded from 7 ChR2-positive mice for monomolecular odorants (dataset 7). The number of cells recorded per animal ranged from 1 to 43. Each stimulus was presented 5 (dataset 3) or 10 (datasets 1, 2, 4, 5, 6 and 7) times. Trials of different odorant stimuli were presented in a pseudorandom manner for all datasets except for the DREADD mice and their control (datasets 5 and 6) as explained above.

Electrophysiological data analysis

All subsequent analyses and statistics were done using custom routines written for Matlab (MathWorks, Inc., Natick, MA).

Breathing cycle realignment—In order to analyze the consistent neural responses to odors across trials, the beginning of each cycle was temporally realigned to each other as previously described [28]. In brief, all breathing cycles in awake animals were artificially matched to the mean breathing duration averaged over all trials: longer cycles were cut and shorter ones were prolonged. We observed an average breathing duration of 336 ± 100 ms for dataset 1, 296 ± 94 ms for dataset 2, 362 ms ± 179 for the dataset 3, 362 ± 100 ms for the ChR2 expressing mice (dataset 4), 334 ± 144 for DREADD expressing mice (dataset 5), 350 ± 145 for ChR2-expressing mice used as control for DREADD (dataset 6) and 308 ± 112 for the ChR2-expressing mice tested with simple odors (dataset 7, all values mean $\pm$ SD). Corresponding spike timings were realigned with the same method. Importantly, relative action potential timings in spike trains were not affected by this method.

Statistical analysis of the rate change for single cell responses—Change of odor-evoked firing rate over the breathing cycle duration was assessed, relative to baseline, by the non-parametric Wilcoxon rank sum (WRS) test repeated in each respiratory cycles spanning stimulus presentation and for all cells and stimuli. Three breathing cycles in the baseline activity were used as a template. The template was compared subsequently to the first three breathing cycles after odor onset. In a particular cycle, a cell was considered as responsive if at least one odorant stimulus evoked a significant change in firing in comparison to baseline. We set the *P*-value to 0.05.

For each significant change, a response was considered as excited if the average firing rate over the complete breathing cycle was significantly higher from the baseline and inhibited if it was significantly lower.

Statistical analysis of the temporal change for single cell responses—Change in the spike timing distribution during odor presentation was assessed by comparing the spike timing relative to the onset of the inspiration before and after odorant presentation using a Kolmogorov-Smirnov (KS) test repeated for each respiratory cycles for all cells and stimuli. Three breathing cycles in the baseline activity were used as a template. The template was compared each consecutive breathing cycles (3 in total) after the odor onset. In a particular cycle, a cell was considered as responsive if at least one odorant stimulus evoked a significant change in firing in comparison to baseline. We set the p value to 0.05.

Population vector construction—We pooled all M/T cells recorded in different animals. The activity of the 78, 169, 130, 38, 55, 40 and 39 (depending on the data set) neurons were organized in 78, 169, 130, 38, 55, 40 and 39 dimensional vectors respectively, containing in each dimension the average firing rate of a recorded cell computed over a certain time bin. Population vectors were built using 1 and 8 bins per breathing cycles (on average, awake: ~42, ~37, ~44, ~36, ~41, ~43ms and ~30 time bins for datasets 1 to 4, respectively).

To test weather noise induced by baseline activity might influence the decorrelation process, we normalized the population vector by subtracting it with averaged activity across 6 breaths during the baseline before the odor onset.

Correlation matrix—The matrix of correlation was built by computing the Pearson coefficient of correlation between pairs of population vectors averaged over the trials evoked by two different odors. The dimensions of the matrix correspond to $n \times n$, where n is the number of odors. Each square corresponds to the Pearson coefficient of correlation of a particular odor against another. The odorants were ranked based on the theoretical ratios of components.

For more accurate detection of the minimum (Fig. 5e), correlations were computed on 21 ms time windows (i.e. 16 bins).

Head-restrained behavioral paradigm

Mice were trained to discriminate odorants under head-fixed paradigm as described previously[19]. In brief, before each behavioral session, a mouse was head-restrained in a plastic tube by screwing the head-post on a custom made holder fixed on a platform (Fig. 5a and Supplementary fig. 9). All behavior experiments were performed using a custom built olfactometer (similar to the ones used for imaging and electrophysiology), which was synchronized to a custom built lickometer. 11 odorant pairs were used for the behavioral training, which was selected from the panel of odorants used for the electrophysiology based on the level of correlation computed on M/T cell population responses.

Habituation task—Beginning 1–3 days after starting the water restriction, animals were trained in an associative task using an operant conditioning procedure. In a first pre-training session, a water drop (2 μL) was presented to animals (40 trials) 3s after a 200 ms-long warning tone (two different frequencies, 5 KHz and 6 KHz, were used on two different setups in the same room). The warning tone was used to make the mice alert about the following stimuli. During this stage, water was delivered to mice without analyzing their licking behavior. During the second stage, following the tone, licking was recorded during the baseline (1 s) as well as during the odor presentation (in this experiment, 1% methyl benzoate). Odors were presented for 2 s. If animals were not licking during the baseline, we implemented the criteria for water delivery based on their licking time during odor presentation. The total licking time required during odor presentation to trigger water reward was gradually increased in each step from 40 ms up to 240 ms (40 ms – 30 trials, 80 ms – 30 trials, 120 ms – 30 trials, 160 ms – 50 trials, 240 ms – 50 trials). If animals were licking during the baseline before odor presentation, the required licking time kept increasing from 100% (same amount of licking as during the baseline) up to 200% (100% – 30 trials, 125% – 30 trials, 150% – 30 trials, 175% – 50 trials, 200% – 50 trials). Most animals learned this task in 2—3 days (4-—6 sessions of 30 min each).

Olfactory discrimination task—The inter-trial interval was constant (13.2 s including the preloading of 3.2 s). Mice were trained to discriminate between two odorants, one being rewarded (S+) and the other being unrewarded (S—). The criterion to get a water reward

was a 80 ms total lick time in three out of four 500 ms time bins during the 2 s odor presentation. If mice licked before odorant presentation, they had to lick double amount of time during the odor presentation to get water reward. Trials were counted as correct if the animals met the criteria mentioned above for rewarded trials. For unrewarded trials, the criterion for a correct trial was a maximum 80 ms lick time in one out of four time bin of 500 ms during the 2 s odor presentation. If mice licked during the baseline of an unrewarded trial, the trial was counted as correct, if the total licking time during 2 s odor presentation did not exceed 25% of their baseline licking. Generally most of the mice did not lick for unrewarded trials and they consistently licked for rewarded trials after the task acquisition. No punishment was given to the mice for incorrect trials.

Odors were presented in a pseudo-randomized order (no more than 2 successive presentations of the same odor, equal numbers within each block of 20 trials, ensuring different order of presentations for S+ and S— trials within each 20 trial blocks). No intrinsic preference toward any of the odors was observed. Bias caused by odor preferences was generally avoided by assigning the same odor as S+ or S— stimulus for the same number of animals within the experimental group. A total of 80—160 trials per session per animal and a total of 150—300 trials per day per animal were performed in order to keep animal motivated. Motivation was checked by monitoring the licking. Mice stopped licking when they lost motivation, in which case the session was interrupted. No animals were excluded for failing to acquire the task. Reaction times were calculated as previously described [19].

The following sequence of tasks were done (Fig. 5): AA vs. EB (2 days), break (19 days), AA60/EB40 vs. AA40/EB40 in air (2 days), break (55 days), HX vs. EB (2 days), break (4 days), HX60/EB40 vs. HX40/EB60 in air (3days), break (4 days), HX60/EB40 vs. HX40/EB60 in liquid (2days), break (6 days), HX60/EB40 vs. AA60/EB40 in air (2days), break (90 days), HX80/EB20 vs. HX20/EB80 in air (2 days), break (81 days), AA80/EB20 vs. AA20/EB80 in air (2days), break (1 day), HX80/EB20 vs. AA80/EB20 in air (1 day), break (2 days), HX40/EB60 vs. AA60/EB40 in air (2 days), break (1 day), AA60/EB40 vs. AA40/EB60 in liquid (2 days).

AAV injection

The skin atop the skull was removed. Using a biopsy punch of 2.5 mm diameter (Harris, Uni-Core, Canada), a piece of bone was removed above the surface of both OBs. While removing the piece of bone, the skull was maintained wet to prevent the dura from sticking to the bone.

Virus injections were done in the granule cell layer of the olfactory bulb following the method described previously[18]. In order to avoid contamination in other cell types or brain regions, we restrained the injection site in the anterior portion of the OB and at an intermediate depth. The zero point was set with respect to the center of the dorsal surface of the OB (see [18]). Starting from this point, four injections were done in the following order: (1) AP: +500 μm, DV: −1000 μm; (2) +300 μm, DV: −1300 μm; (3) +100 μm; DV: −1400 μm; (4) +100 μm; DV: −2000 μm. 100—150 μL of AAV1—ACAGW—ChR2—Venus, AAV5—EF1—eGFP.WRPE.RBG or rAAV2—hSyn—HA—hM4D(Gi)—IRES—mCitrine

(University of North Carolina vector core facility) were injected by keeping the injection time around 2—3 min. We waited at least 5 min before removing the injection pipette in order to avoid diffusion of the virus toward the surface.

Optogenetic and pharmacogenetic manipulation of behavior

Cranial window implantation—The skull surrounding the hole was thinned to fit a cover glass. A drop of dexamethasone, a glucocorticoid steroid, was applied on the surface of the dura to minimize possible inflammation. After few minutes, the dexamethasone was cleaned with cortex buffer (containing in mM 125 NaCl, 10 glucose, 10 HEPES, 5 KCl, 2 $CaCl_2$, 2 $MgCl_2$). A drop of clean cortex buffer was put on the OB surface before placing the cover glass. A 3mm diameter cover glass was fitted in the hole on top of OB. Excessive cortex buffer was dried around the window until the surrounding bone was completely dry. The edge of the window was sealed with dental cement (Palladur mixed with Palapress vario, Pala). Once the window was fixed, we implanted the head-post as previously described[13,18,28]. A delay of at least 3 weeks was respected in order to obtain an optimal ChR2 expression. After this period, we checked the transparency of the cranial windows and a ~2mm diameter blue LED (blue LED, NFSB036BT) with the connector (ED8250-ND, connector strip header 50POS .050, Millmax) was implanted on top of the window with dental cement (Palladur mixed with Palapress vario, Pala). The LED illuminated a surface of ~5.3 mm^2 covering both bulbs.

Settings of LED power—During the optogenetic behavior experiments, the implanted LEDs were driven with a high power LED driver (LEDD1B, T-Cube LED Driver 1200 mA, ThorLabs). The goal of the experiment was to evaluate whether the photoactivation of GCL neurons could enhance odorant discrimination. However, overstimulation of the inhibitory network may shut down the M/T cells activity. As the degree of ChR2 infection could vary between different animals, the maximum power needed to shut down OB activity may also vary. For this reason, we set a maximum light power that would be optimal for each mouse. We pre-trained the animals until they learned to lick sufficiently during odorant application[19]. We then photo-activated the network during odor application using a light power that blocked the licking behavior (Supplementary Fig. 9). The maximum power needed to shut down the odor-evoked licking behavior was 23 mW (7.3 mW/mm^2) for ChR2-expressing mice. Finally, we applied the same sequence of blocks by gradually reducing the light power for each individual mouse until they showed a similar licking pattern as observed without light stimulation. This power varied for individual mice and was used for the stimulation of granule cells during the go/no-go discrimination tasks.

Light driven discrimination behavior paradigm—During optogenetic behavior experiments, we monitored the breathing cycles using an air flow sensor (AWM2100V, Honeywell, MN) coupled with a home-made amplifier in order to precisely set odorant and light onset based on the respiratory time course. The odorant onset began at the end of the mouse inspiration and lasted for 2 seconds. The light onset started at the beginning of inspiration along with odorant trigger. We used 80 pulses of 5ms at a frequency of 40hz. As mentioned in the previous section, the power was individually set for each mouse. The discrimination training was carried out as described previously.

Injection of clozapine-N-oxide (CNO)—CNO diluted in saline was prepared freshly every day. After isoflurane anesthesia, each mouse (DREADD and ChR2 expressing mice) was injected with 2 mg/kg 15—20 minutes before the animal started the discrimination paradigm. Mice performed the task for a maximum of 60—75 min after the injection.

Immunohistochemistry and quantification

Animals were anaesthetized by intraperitoneal injection of urethane 20% in 0.9% NaCl and perfused transcardially with 40 ml of saline followed by 100 ml of 4% paraformaldehyde (PFA) in 0.1M phosphate buffer at 4°C (PBS, pH 7.3). The brains were then removed and fixed overnight in 4% PFA. After embedding brains in 4% agarose, 40 μm coronal slices were cut with a vibratome (Leica VT S1000) and collected in PBS (0.1 M). For immunostaining, we first rinsed in TBST (Tris-buffered saline with tween) and TBSTT (Tris-buffered saline with tween and triton). We incubated the slices with 10% bovine serum for 1h at room temperature and then with the primary antibodies overnight at 4°C. We used a rabbit anti-GFP antibody[29] (1:1000, Invitrogen A11122), a mouse anti-Reelin antibody[29] (1:1000, Abcam 78540) and a mouse anti-NeuN antibody[29] (1:500, Millipore MAB377). The day after, slices were rinsed with TBST and incubated with Alexa 488 anti-rabbit IgG[29] (1:200, Invitrogen, A21206) and Alexa 546 anti-mouse IgG[29] (1:200, Invitrogen, A21123) for 1h at room temperature. Slices were counterstained with Hoechst 154 (1:5000, Invitrogen, H3570) and mounted with Vectashield (Vectors Laboratories).

Images were acquired with a confocal laser scanning microscope (Zeiss LSM 510META and Leica SPM5) with a 40× or 63× oil-immersion objectives. Fluorescent channels were acquired sequentially to separate wavelength and minimize possible cross-talk. In the MCL and GL, all slices were visually inspected in order to find GFP/mCitrine positive neurons. Since we could not find any, only few slices were scanned for illustration. In the GCL, counting was done manually with ImageJ on 75 and 42 representative regions of 26 and 22 slices in the anterior, medial and posterior part of the OB for ChR2 and Gi-DREADD infected mice, respectively ($n = 6$ animals for each group; Supplementary Fig. 8). In total, ~25000 cells were analyzed.

Statistics

All analyses were performed using Matlab (MathWorks, Inc., Natick, MA), Origin pro, Statistica or Prism. In this study, we used ANOVA and post-hoc tests, χ^2 test and different non-parametric tests (see text and legends). All tests were 2-sided. Shapiro-Wilk test was used to assess normality of the data. For all parametric ANOVA, homogeneity of variance was tested using Levene's test or a test of sphericity (for one-way repeated measures ANOVA). No statistical methods were used to predetermine sample sizes, but our sample sizes were similar to those reported in previous publications[13,19,28,29]. Data collection and animal assignation to the various experimental groups were randomized.

Supplementary Material

Refer to Web version on PubMed Central for supplementary material.

ACKNOWLEDGEMENTS

REFERENCES

1. Friedrich RW, Laurent G. Dynamic optimization of odor representations by slow temporal patterning of mitral cell activity. Science (New York, N.Y). 2001; 291:889–894. [PubMed: 11157170]

2. Friedrich RW, Laurent G. Dynamics of olfactory bulb input and output activity during odor stimulation in zebrafish. Journal of neurophysiology. 2004; 91:2658–2669. [PubMed: 14960561]

3. Niessing J, Friedrich RW. Olfactory pattern classification by discrete neuronal network states. Nature. 2010; 465:47–52. [PubMed: 20393466]

4. Barnes DC, Hofacer RD, Zaman AR, Rennaker RL, Wilson DA. Olfactory perceptual stability and discrimination. Nature neuroscience. 2008; 11:1378–1380. [PubMed: 18978781]

5. Chapuis J, Wilson DA. Bidirectional plasticity of cortical pattern recognition and behavioral sensory acuity. Nature neuroscience. 2012; 15:155–161. [PubMed: 22101640]

6. Leutgeb JK, Leutgeb S, Moser MB, Moser EI. Pattern separation in the dentate gyrus and CA3 of the hippocampus. Science (New York, N.Y). 2007; 315:961–966. [PubMed: 17303747]

7. McHugh TJ, et al. Dentate gyrus NMDA receptors mediate rapid pattern separation in the hippocampal network. Science (New York, N.Y). 2007; 317:94–99. [PubMed: 17556551]

8. Nakashiba T, et al. Young dentate granule cells mediate pattern separation, whereas old granule cells facilitate pattern completion. Cell. 2012; 149:188–201. [PubMed: 22365813]

9. Friedrich RW. Neuronal computations in the olfactory system of zebrafish. Annu Rev Neurosci. 2013; 36:383–402. [PubMed: 23725002]

10. Friedrich RW, Wiechert MT. Neuronal circuits and computations: pattern decorrelation in the olfactory bulb. FEBS Lett. 2014; 588:2504–2513. [PubMed: 24911205]

11. Rolls ET. The mechanisms for pattern completion and pattern separation in the hippocampus. Front Syst Neurosci. 2013; 7:74. [PubMed: 24198767]

12. Vincis R, Gschwend O, Bhaukaurally K, Beroud J, Carleton A. Dense representation of natural odorants in the mouse olfactory bulb. Nature neuroscience. 2012; 15:537–539. [PubMed: 22406552]

13. Patterson MA, Lagier S, Carleton A. Odor representations in the olfactory bulb evolve after the first breath and persist as an odor afterimage. Proceedings of the National Academy of Sciences of the United States of America. 2013; 110:E3340–3349. [PubMed: 23918364]

14. Abraham NM, et al. Maintaining accuracy at the expense of speed; stimulus similarity defines odor discrimination time in mice. Neuron. 2004; 44:865–876. [PubMed: 15572116]

15. Linster C, Johnson BA, Morse A, Yue E, Leon M. Spontaneous versus reinforced olfactory discriminations. J Neurosci. 2002; 22:6842–6845. [PubMed: 12177181]

16. Linster C, et al. Perceptual correlates of neural representations evoked by odorant enantiomers. J Neurosci. 2001; 21:9837–9843. [PubMed: 11739591]

17. Rubin BD, Katz LC. Spatial coding of enantiomers in the rat olfactory bulb. Nature neuroscience. 2001; 4:355–356. [PubMed: 11276223]

18. Abraham NM, et al. Synaptic inhibition in the olfactory bulb accelerates odor discrimination in mice. Neuron. 2010; 65:399–411. [PubMed: 20159452]

19. Abraham NM, Guerin D, Bhaukaurally K, Carleton A. Similar odor discrimination behavior in head-restrained and freely moving mice. PLoS One. 2012; 7:e51789. [PubMed: 23272168]

20. Abraham NM, Vincis R, Lagier S, Rodriguez I, Carleton A. Long term functional plasticity of sensory inputs mediated by olfactory learning. eLife. 2014; 3:e02109. [PubMed: 24642413]

21. Stettler DD, Axel R. Representations of odor in the piriform cortex. Neuron. 2009; 63:854–864. [PubMed: 19778513]

22. Miura K, Mainen ZF, Uchida N. Odor representations in olfactory cortex: distributed rate coding and decorrelated population activity. Neuron. 2012; 74:1087–1098. [PubMed: 22726838]

23. Wiechert MT, Judkewitz B, Riecke H, Friedrich RW. Mechanisms of pattern decorrelation by recurrent neuronal circuits. Nature neuroscience. 2010; 13:1003–1010. [PubMed: 20581841]

24. Schaefer AT, Margrie TW. Spatiotemporal representations in the olfactory system. Trends Neurosci. 2007; 30:92–100. [PubMed: 17224191]

25. Cury KM, Uchida N. Robust odor coding via inhalation-coupled transient activity in the mammalian olfactory bulb. Neuron. 2010; 68:570–585. [PubMed: 21040855]

26. Rinberg D, Koulakov A, Gelperin A. Speed-accuracy tradeoff in olfaction. Neuron. 2006; 51:351–358. [PubMed: 16880129]

27. Uchida N, Mainen ZF. Speed and accuracy of olfactory discrimination in the rat. Nature neuroscience. 2003; 6:1224–1229. [PubMed: 14566341]

28. Gschwend O, Beroud J, Carleton A. Encoding odorant identity by spiking packets of rate-invariant neurons in awake mice. PLoS ONE. 2012; 7:e30155. [PubMed: 22272291]

29. Tatti R, et al. A population of glomerular glutamatergic neurons controls sensory information transfer in the mouse olfactory bulb. Nature communications. 2014; 5:3791.

30. Arevian AC, Kapoor V, Urban NN. Activity-dependent gating of lateral inhibition in the mouse olfactory bulb. Nature neuroscience. 2008; 11:80–87. [PubMed: 18084286]

31. Giridhar S, Doiron B, Urban NN. Timescale-dependent shaping of correlation by olfactory bulb lateral inhibition. Proceedings of the National Academy of Sciences of the United States of America. 2011; 108:5843–5848. [PubMed: 21436050]

32. Koulakov AA, Rinberg D. Sparse incomplete representations: a potential role of olfactory granule cells. Neuron. 2011; 72:124–136. [PubMed: 21982374]

33. Bathellier B, Buhl DL, Accolla R, Carleton A. Dynamic ensemble odor coding in the mammalian olfactory bulb: sensory information at different timescales. Neuron. 2008; 57:586–598. [PubMed: 18304487]

34. Guerrieri F, Schubert M, Sandoz JC, Giurfa M. Perceptual and neural olfactory similarity in honeybees. PLoS Biol. 2005; 3:e60. [PubMed: 15736975]

35. Youngentob SL, et al. Experience-induced fetal plasticity: the effect of gestational ethanol exposure on the behavioral and neurophysiologic olfactory response to ethanol odor in early postnatal and adult rats. Behav Neurosci. 2007; 121:1293–1305. [PubMed: 18085882]

36. Friedrich RW, Habermann CJ, Laurent G. Multiplexing using synchrony in the zebrafish olfactory bulb. Nature neuroscience. 2004; 7:862–871. [PubMed: 15273692]

37. Yaksi E, Judkewitz B, Friedrich RW. Topological reorganization of odor representations in the olfactory bulb. PLoS Biol. 2007; 5:e178. [PubMed: 17608564]

38. Kato HK, Gillet SN, Peters AJ, Isaacson JS, Komiyama T. Parvalbumin-expressing interneurons linearly control olfactory bulb output. Neuron. 2013; 80:1218–1231. [PubMed: 24239124]

39. Miyamichi K, et al. Dissecting local circuits: parvalbumin interneurons underlie broad feedback control of olfactory bulb output. Neuron. 2013; 80:1232–1245. [PubMed: 24239125]

40. Cleland TA, Sethupathy P. Non-topographical contrast enhancement in the olfactory bulb. BMC neuroscience. 2006; 7:7. [PubMed: 16433921]

41. Fukunaga I, Herb JT, Kollo M, Boyden ES, Schaefer AT. Independent control of gamma and theta activity by distinct interneuron networks in the olfactory bulb. Nature neuroscience. 2014; 17:1208–1216. [PubMed: 24997762]

42. Chow SF, Wick SD, Riecke H. Neurogenesis drives stimulus decorrelation in a model of the olfactory bulb. PLoS Comput Biol. 2012; 8:e1002398. [PubMed: 22442645]

43. Linster C, Cleland TA. Decorrelation of Odor Representations via Spike Timing-Dependent Plasticity. Frontiers in computational neuroscience. 2010; 4:157. [PubMed: 21228906]

44. Alonso M, et al. Activation of adult-born neurons facilitates learning and memory. Nature neuroscience. 2012; 15:897–904. [PubMed: 22581183]

45. Carleton A, et al. Making scents of olfactory neurogenesis. J Physiol Paris. 2002; 96:115–122. [PubMed: 11755790]

46. Padmanabhan K, Urban NN. Intrinsic biophysical diversity decorrelates neuronal firing while increasing information content. Nature neuroscience. 2010; 13:1276–1282. [PubMed: 20802489]

47. Boyd AM, Sturgill JF, Poo C, Isaacson JS. Cortical feedback control of olfactory bulb circuits. Neuron. 2012; 76:1161–1174. [PubMed: 23259951]

48. Markopoulos F, Rokni D, Gire DH, Murthy VN. Functional properties of cortical feedback projections to the olfactory bulb. Neuron. 2012; 76:1175–1188. [PubMed: 23259952]

49. Haddad R, et al. Olfactory cortical neurons read out a relative time code in the olfactory bulb. Nature neuroscience. 2013; 16:949–957. [PubMed: 23685720]

50. Wilson DA, Sullivan RM. Cortical processing of odor objects. Neuron. 2011; 72:506–519. [PubMed: 22099455]

Supplementary references

51. Li J, Ishii T, Feinstein P, Mombaerts P. Odorant receptor gene choice is reset by nuclear transfer from mouse olfactory sensory neurons. Nature. 2004; 428:393–399. [PubMed: 15042081]

52. Zariwala HA, et al. A Cre-dependent GCaMP3 reporter mouse for neuronal imaging in vivo. J Neurosci. 2012; 32:3131–3141. [PubMed: 22378886]

53. Bathellier B, Van De Ville D, Blu T, Unser M, Carleton A. Wavelet-based multi-resolution statistics for optical imaging signals: Application to automated detection of odour activated glomeruli in the mouse olfactory bulb. Neuroimage. 2007; 34:1020–1035. [PubMed: 17185002]

54. de Saint Laumer J-Y, Cicchetti E, Merle P, Egger J, Chaintreau A. Quantification in Gas Chromatography: Prediction of Flame Ionization Detector Response Factors from Combustion Enthalpies and Molecular Structures. Analytical Chemistry. 2010; 82:6457–6646. [PubMed: 20698579]

55. Lagier S, Carleton A, Lledo PM. Interplay between local GABAergic interneurons and relay neurons generates gamma oscillations in the rat olfactory bulb. J Neurosci. 2004; 24:4382–4392. [PubMed: 15128852]

56. Lagier S, et al. GABAergic inhibition at dendrodendritic synapses tunes gamma oscillations in the olfactory bulb. Proceedings of the National Academy of Sciences of the United States of America. 2007; 104:7259–7264. [PubMed: 17428916]
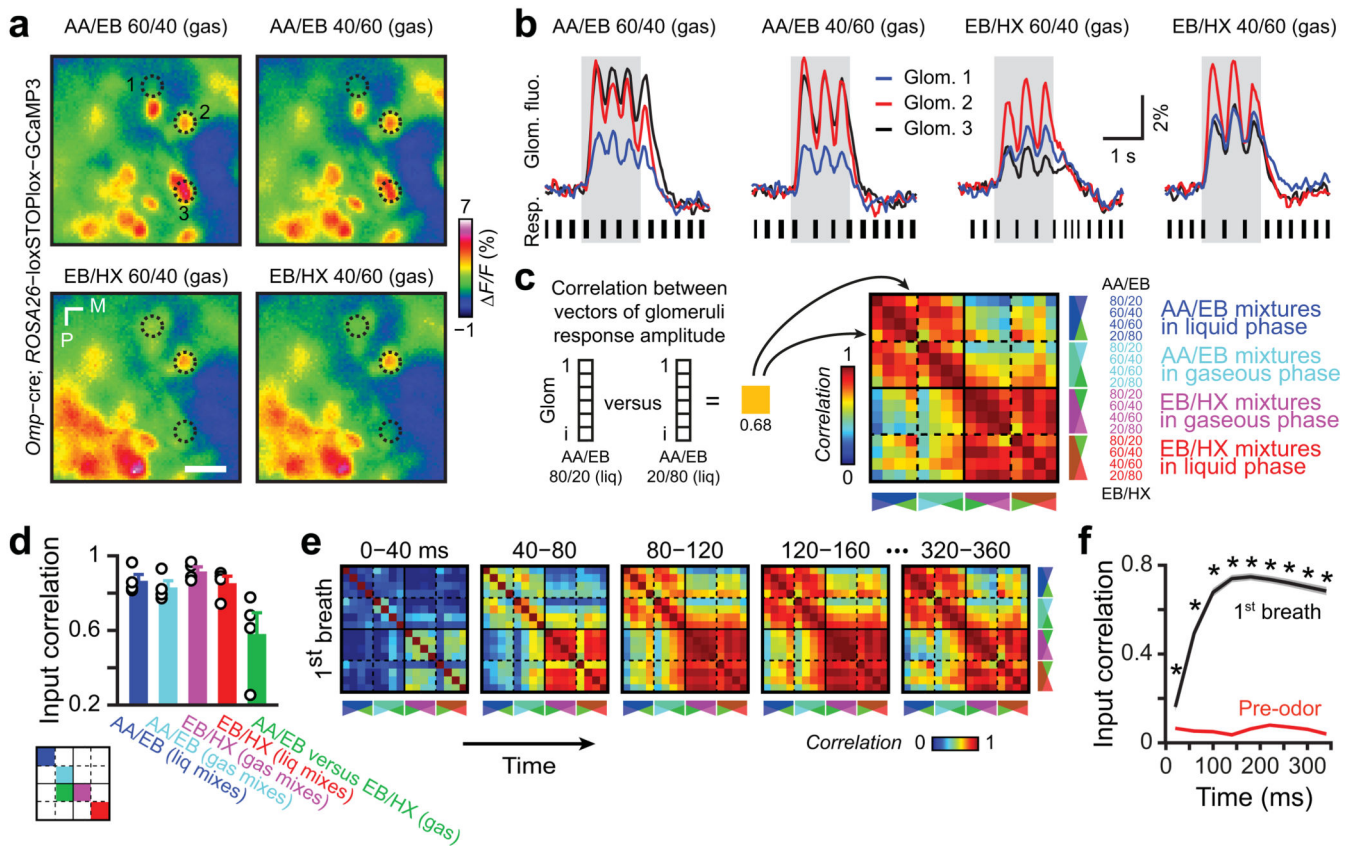
Figure 1.

Binary mixtures evoke correlated input patterns to the mouse olfactory bulb. (**a**) Glomeruli maps evoked by different binary mixtures in the same awake head-restrained mouse (EB: ethyl butyrate, AA: amyl acetate, HX: 3-Hexanone; numbers indicate relative ratio of the components [in %] mixed in gaseous phase, see Supplementary Table 1). The fluorescence from the calcium indicator GCaMP3 genetically expressed in olfactory sensory neurons was monitored on the dorsal surface of the olfactory bulb. Change in fluorescence (F/F) was averaged over 1.5 s odor application (single trial response). Dashed lines indicate three regions of interest (ROIs) activated by the mixtures. (**b**) Calcium dynamics in sensory neuron terminals from the glomeruli ROIs drawn in **a** (single trial, gray boxes: odor presentation). Fluctuation of fluorescence corresponds to different breaths during odor application (see resp.: respiration traces; black bars indicate duration of inspirations). (**c**) Average matrix of input similarity computed for all possible mixtures tested. For each mouse and for each pair of mixtures, Pearson correlation coefficient is computed using two vectors of glomeruli ROI representing calcium changes (F/F, averaged on the first breath) evoked by the two mixtures (note that the matrix is symmetric). The matrix represents the average of correlation matrices computed over the 1st breathing cycle for each mouse ($n = 4$). The components and theoretical ratios used in different mixtures are indicated. Plain lines separate mixtures having different components (AA/EB vs EB/HX). Dashed lines separate mixtures having the same components but with differing mixing procedures (i.e. either in gaseous or in liquid phase). (**d**) Bar graph showing the average correlation for different

subgroups of mixtures as represented by the color code on the left schematic matrix (data presented as mean ± sem, $n = 4$ mice, each circle represents the value for a given animal). For clarity, few subgroups of mixtures have been omitted. Mixtures evoked similar patterns though mixtures having different components were less correlated (Friedman ANOVA $\chi^2 = 10$, $P = 0.04$, post-hoc Wilcoxon paired test: all $P > 0.068$). (**e**) Correlation matrices computed over 40 ms time window across the first breath after odor onset (few matrices have been ommitted for clarity). (**f**) Evolution of the correlation averaged over all odor pairs during the last pre-odor breath and the first breath after odor onset (data presented as mean ± sem; Wilcoxon paired test, at least $*P < 10^{-5}$). During the first breath, after correlation reached a maximum (~120ms), it remained stable over time (Friedman ANOVA $\chi^2 = 13.2$, $P = 0.15$).
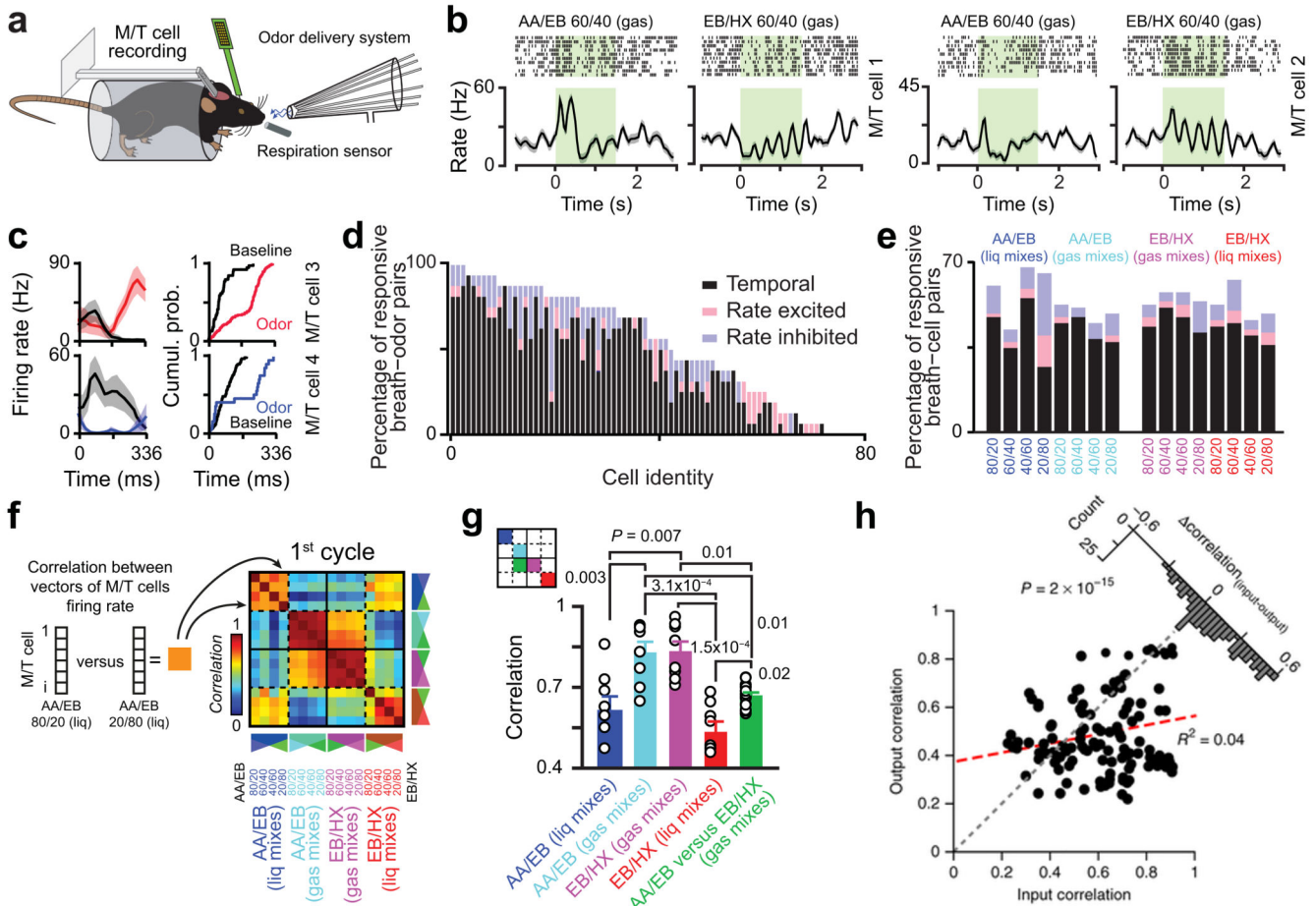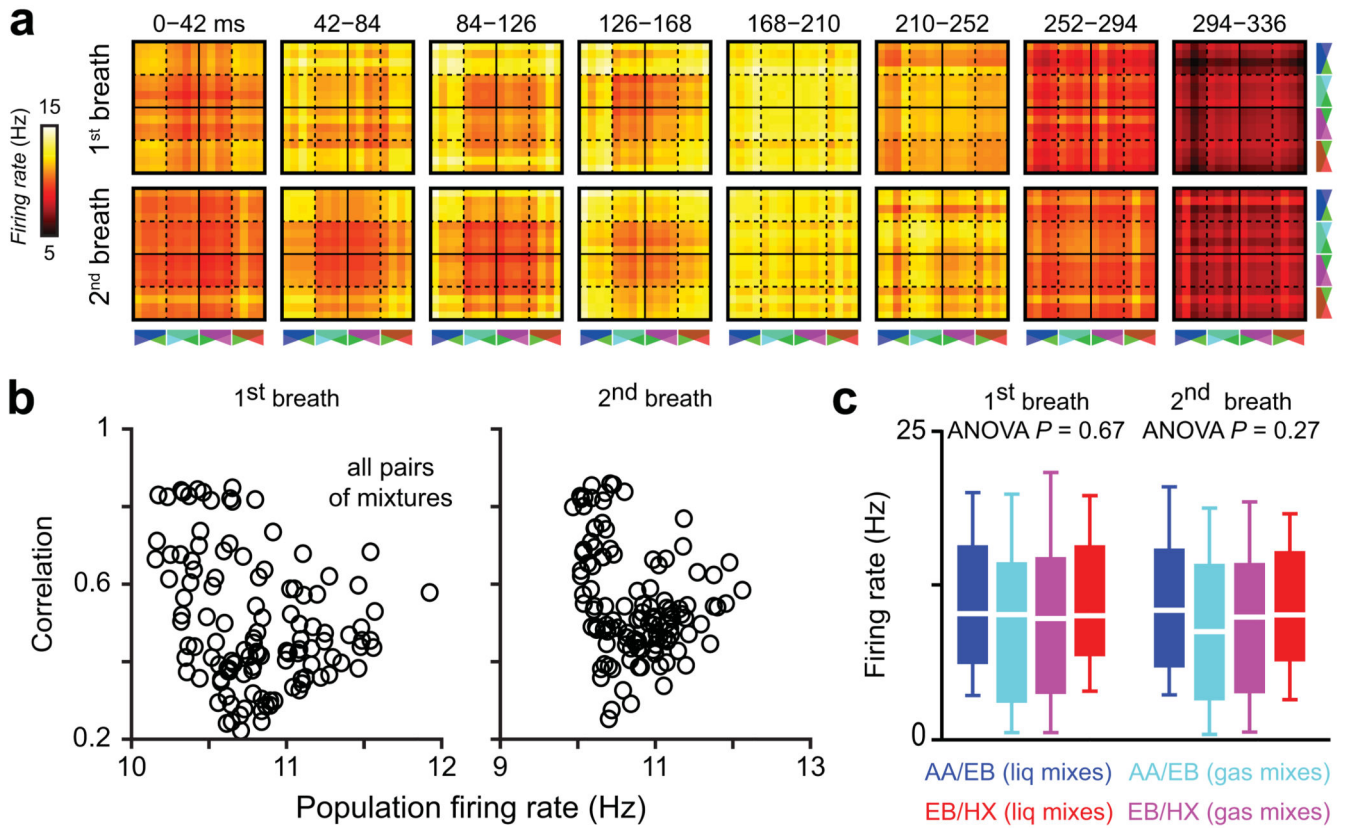
Figure 2.

Input/output reformatting of odor-evoked representations in the OB. (**a**) Schema of the recording procedure. Tetrode recordings of OB output neurons (i.e. mitral/tufted cells, M/T) are done in awake head-restrained mice while presenting odorant mixtures and monitoring breathing. (**b**) Raster plots and peristimulus time histograms (PSTHs, thick line: mean, gray surface: sem) showing the response of two cells to different mixtures (green boxes indicate odor application; 10 trials are shown for each odor/cell). (**c**) Examples of PSTHs (left panels) and corresponding spike distributions (right panels) computed over different breathing cycles for two different cells during baseline (grey lines, three breaths before odor onset averaged) and 1st cycle after odor onset (colored lines). Colored surfaces represent standard deviation. Neurons 3 and 4 are excited and inhibited, respectively. (**d**) Percentage of responsive odor-breath pairs for the neurons recorded in the first dataset (same odors as in **e**). (**e**) Percentage of responsive cell-breath pairs for each odor. Neurons displaying an increase in firing rate (averaged on the entire breath), a decrease in firing rate or only a change of spike distribution (temporal change) between baseline and odor epochs are presented in red, blue and black, respectively. (**f**) Matrix of output patterns similarity computed for all possible mixtures tested. For each pair of mixtures, pearson correlation coefficient is computed using two vectors of ouput neurons firing rate averaged over the 1st breath after odorant onset evoked by the two mixtures (78 neurons combined). (**g**) Bar graph

showing the average correlation computed over the first breath after odor onset for selected subgroups of mixtures (same groups as in Fig. 1d, same color code as in **f**; data are presented as mean ± sem; Mann-Whitney test; each circle represents a correlation value between pairs of mixtures). (**h**) Relationship between inputs and outputs correlations for all tested odor pairs. Each point represents the input/output correlations for a given mixture pair (1st dataset, 112 pairs of mixtures). Output correlations are significantly reduced in comparison to input correlations (Kolmogorov-Smirnov KS test). The histogram (top right) shows the distribution of difference between input and output correlations evoked by the same mixture pair. The distribution is skewed toward positive values, indicating more decorrelated values for the output patterns.
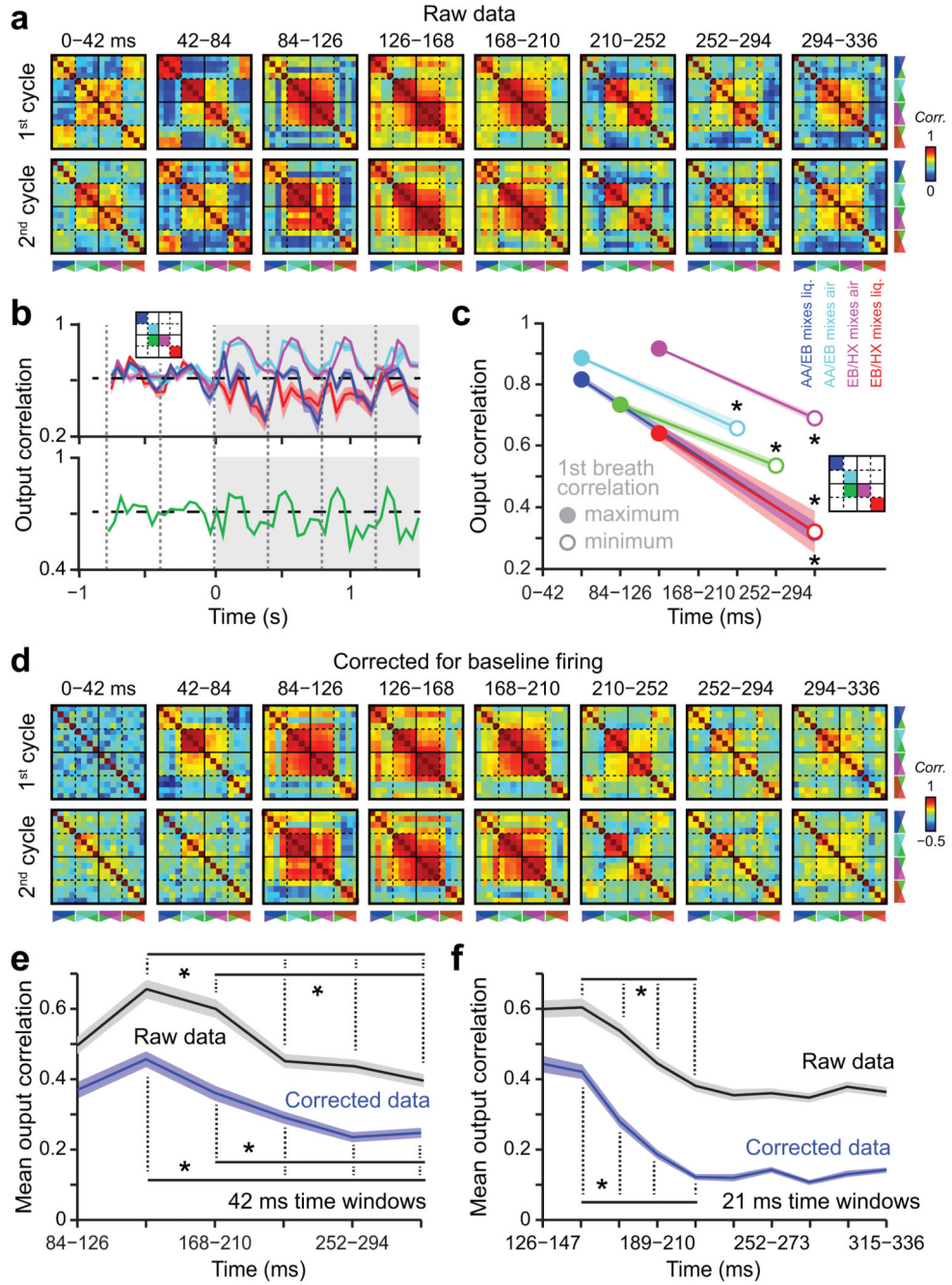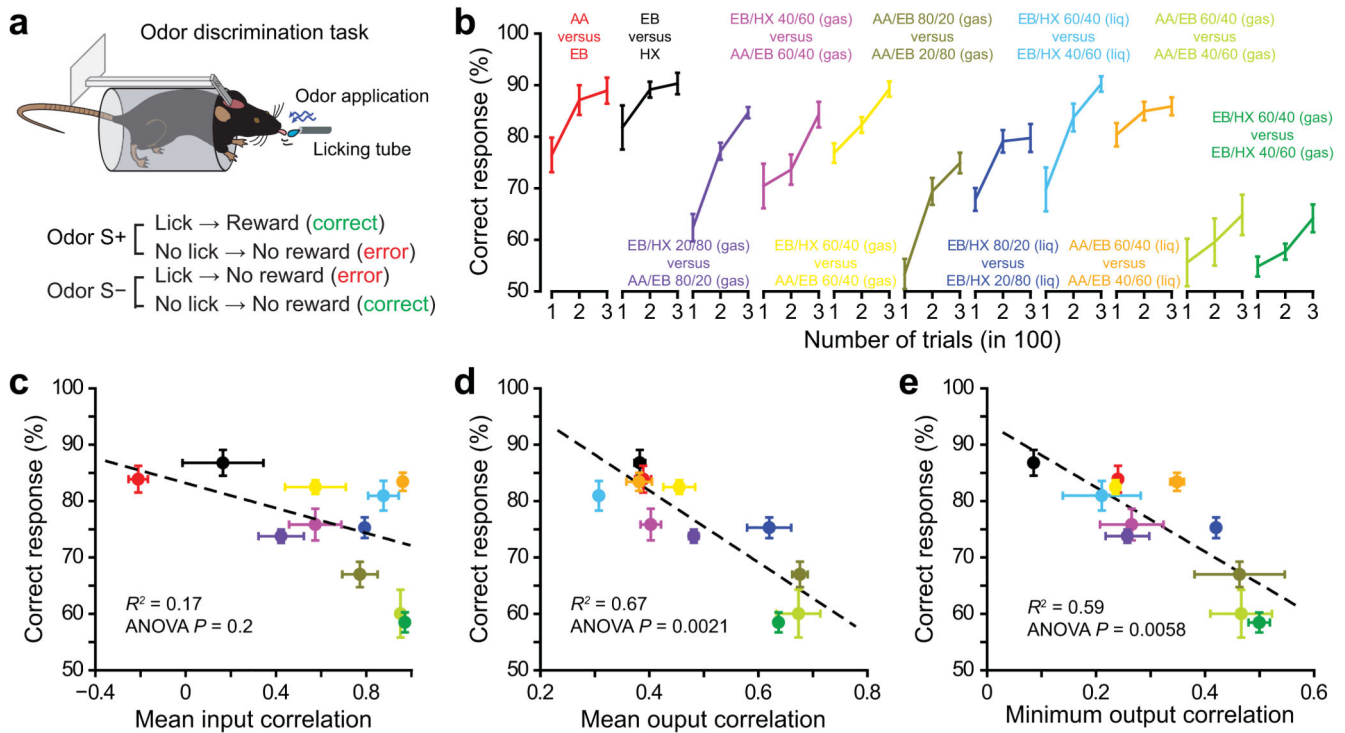
Figure 3.
Odor-specific separation of output patterns over a single breath. (**a**) Temporal evolution of the correlations for all possible pairs of mixtures during different breathing cycles after odor onset. Correlation matrices are computed using vectors of firing rate averaged over consecutive 42 ms time windows. (**b**) Average correlation for different subgroups of mixtures plotted over time (grey boxes indicate odor application; thick line: mean, colored surface: sem; dashed lines indicate inspiration onset). Mixtures sharing components and having different components are shown on the top and bottom plots, respectively. The color

codes correspond to the different groups shown on the schematic matrix. For clarity, few subgroups of mixtures are not plotted. Note that correlations significantly change over the time course of the breaths (for each subgroup of mixtures: Friedman ANOVA computed on the first breath, $P = 0.0007$). (**c**) Amplitude and first breath timing of the maximum and minimum of correlation computed for different subgroups of mixtures. Note a significant decorrelation for all groups (Wilcoxon paired test, at least *$P < 0.0022$). (**d**) Temporal evolution of the correlations in the first breath for the same data but corrected for the baseline firing. For each time window, the activity of each cell during the odor period was corrected by subtracting its baseline breath activity (averaged over 6 breath pre-odor onset). (**e**) Temporal evolution of the correlation computed on 42 ms time windows and averaged across all mixtures for the raw and corrected data. For clarity, many significant comparisons have been omitted (Wilcoxon paired test, at least *$P < 0.001$). (**f**) Same analysis as in **e** but for correlation computed on 21 ms time windows. Data presented as mean ± sem
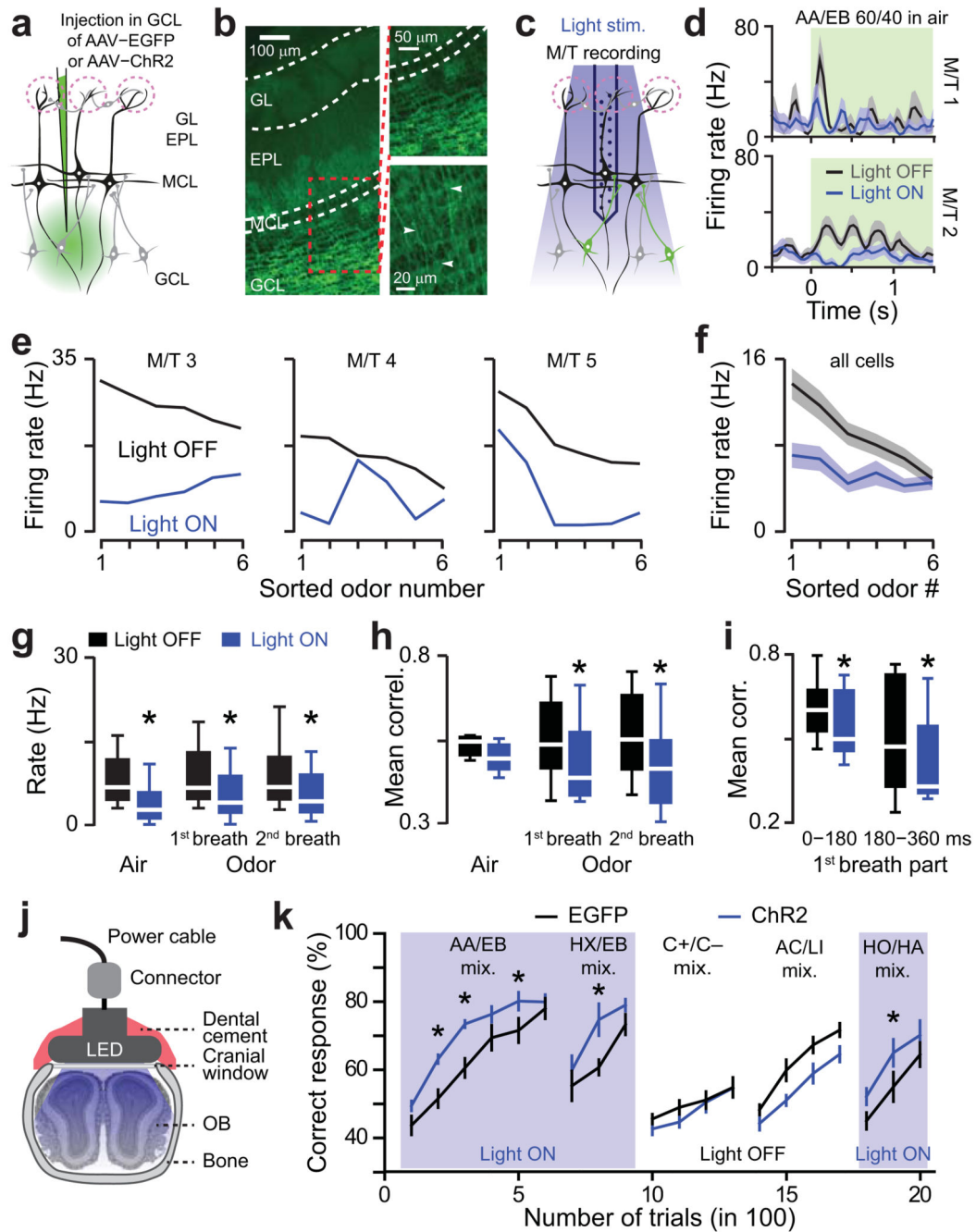
Figure 4.
Population firing rate does not predict output correlations. (**a**) Temporal evolution of the population firing rate for all possible pairs of mixtures during different breathing cycles after odor onset. Each pixel represents the averaged population firing rate evoked by two mixtures. The organization of the matrices is similar to the one of correlation matrices (see Fig. 2). (**b**) Output correlation plotted as a function of the population firing rate (averaged over the entire breath) for all possible mixture pairs. Scatter plots for the first two breaths after odor onset are shown. (**c**) Odor-evoked population firing rate averaged over all cells (n = 78) is not different between subgroups of mixtures. Data are presented as box plots (25th and 75th percentiles) showing the mean in white. Whiskers represent the 10th and 90th percentiles.
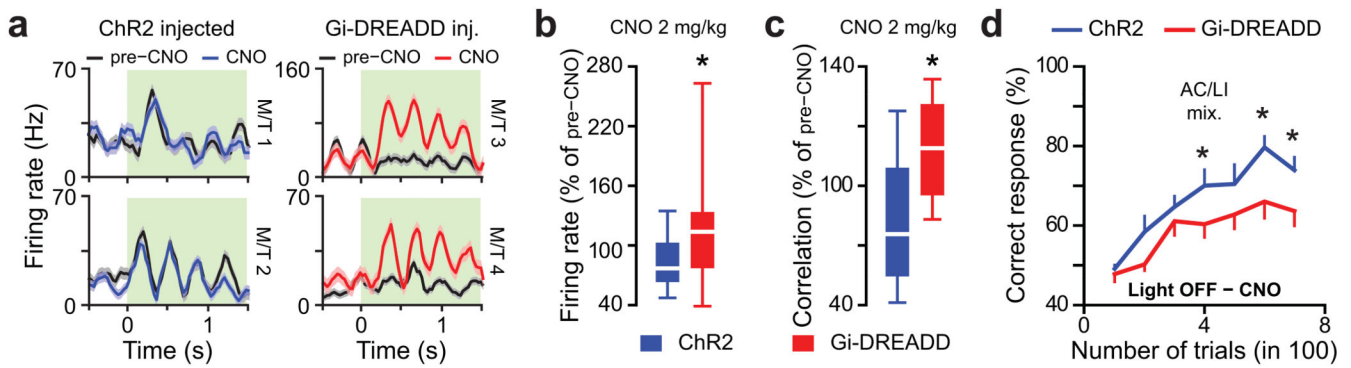
Figure 5.

OB output but not input patterns correlation predicts odor discrimination performances. (**a**) Schema of odor discrimination tasks performed in head-restrained mice. Mice are trained to discriminate between two odors, one rewarded (S+) and one unrewarded (S−). For each task, the selection of S+ and S− odors is balanced across animals. (**b**) Average discrimination performances for different pairs of odorants (*n* = 18 mice for AA/EB 60/40 vs AA/EB 40/60 in gaseous phase and EB/HX 60/40 vs EB/HX 40/60 in gaseous phase, *n* = 12 mice for all other tasks). Odor pairs are organized according to their input correlation (lowest correlation in the left). (**c-e**) The discrimination performance averaged over 300 trials is plotted as a function of the mean input pattern correlation (**c**), the mean output pattern correlation (**d,** correlation values computed for the 1st odor cycle from datasets 1 to 3 are averaged, error bars represent sem) or the minimum output correlation (**e**) for several odor pairs (same color code as in **b**; correlation values computed for the 1st odor cycle from datasets 1 to 3 have been averaged, error bars represent sem). Linear regressions are indicated in dashed lines. Data are presented as mean ± sem.

Figure 6.

Optogenetic stimulation of granule cell layer neurons enhances pattern separation and improves odor discrimination learning. (**a**) Schema of the virus injection procedure in the granule cell layer (GCL). EPL: external plexiform layer, MCL: mitral cell layer, GL: glomerular layer. (**b**) Specific ChR2-YFP expression in neurons of the GCL (left and top right images). White arrows point to GC apical dendrites (bottom right image). (**c**) Schematic of the recording strategy. An optrode is lowered into the MCL and surrounding ChR2-expressing cells are stimulated with 473nm light. (**d**) PSTHs of odor-evoked response

for two cells in presence or absence of light stimulation (green boxes indicate odor application and light stimulation). (**e**) Odor tuning curves with (blue) and without (black) photostimulation for three M/T cells. For each neuron, the stimuli are sorted based on decreasing odor-evoked firing rates computed on the 1st breath after odor onset in absence of photostimulation. The same order is maintained to plot the curve during photostimulation. Note that photostimulation does not trigger the same effect for all tested odors. (**f**) The population tuning curve represents the average of the tuning curves computed for all recorded neurons ($n = 38$). (**g**) Effect of GCL photostimulation (i.e. light on vs. light off) on the mean population firing rate computed on 228 odor-cell pairs (from $n = 7$ mice) during baseline (3 breaths are averaged; Wilcoxon paired test *$P = 0.002$) and odor application (Wilcoxon paired test *$P = 0.031$). Data are presented as box plots (25th and 75th percentiles) showing the mean in white. Whiskers represent the 10th and 90th percentiles. Odors used (mixed in gaseous phase): AA/EB 60/40, AA/EB 40/60, EB/HX 60/40, EB/HX 40/60, carvone+/carvone− 60/40, C+/C− 40/60, AC/LI 60/40 vs. AC/LI 40/60 and HO/HA 60/40 vs HO/HA 40/60. (**h**) Effect of GCL photostimulation on the mean population correlation (averaged across the pairs taken from 6 odors) during baseline (air, 3 breaths were averaged; Wilcoxon paired test $P = 0.23$) and odor application (Wilcoxon paired test *$P = 0.0054$ and 0.0001). Data are presented as box plots (25th and 75th percentiles) showing the mean in white. Whiskers represent the 10th and 90th percentiles. (**i**) Correlation averaged over the 1st and 2nd half of the 1st breath after odor onset with and without photostimulation (significant decrease between first and second part of the cycle, Wilcoxon paired test $P = 0.01$). Photostimulation evoked a significant decrease of the correlation in both halves of the breath (Wilcoxon paired test, 1st part: $P = 0.016$; 2nd part $P = 0.026$). Data are presented as box plots (25th and 75th percentiles) showing the mean in white. Whiskers represent the 10th and 90th percentiles. (**j**) Schema of a 473nm LED implanted on top of a cranial window overlaying the dorsal OB used for optogenetic stimulation during odor discrimination behavior. (**k**) Discrimination performances for different groups of mice, which received injection of AAV (expression of either ChR2 or EGFP) in the GCL. Performances of ChR2-expressing mice (blue lines, $n = 7$) is specifically improved by photostimulation in comparison to EGFP expressing mice (black lines, $n = 7$; Light ON: repeated measures ANOVA, $F = 8.3$, $P = 0.015$, post-hoc Fischer test at least *$P < 0.034$; Light OFF: repeated measures ANOVA, $F = 3.7$, $P = 0.08$). Blue boxes indicate light ON episodes. The odor pairs used were (all gas mixes): AA/EB 60/40 vs. AA/EB 40/60, EB/HX 60/40 vs. EB/HX 40/60, C+/C− 60/40 vs. C+/C− 40/60, AC/LI 60/40 vs. AC/LI 40/60 and HO/HA 60/40 vs HO/HA 40/60.

Figure 7.

Pharmacogenetic inhibition of granule cell layer neurons decreases pattern separation and deteriorates odor discrimination learning. (**a**) PSTHs of odor-evoked responses before (*black lines*) and after CNO injection (*blue and red lines*) for four cells recorded in mice either infected with AAV-ChR2 or AAV-Gi-DREADD. Green boxes indicate odor application. Odors used: AA/EB 40/60 for M/T cells 1 and 2, AA/EB 60/40 for M/T cell 3 and HX/EB 40/60 for M/T cells 4 (all gas mixes). (**b**) Effect of CNO injection on odor-evoked firing (normalized to the pre-CNO control period) in ChR2- and Gi-DREADD- expressing mice (n = 40 cells recorded from 4 ChR2 mice and 55 cells recorded from 5 Gi-DREADD mice, population vectors computed for 6 different odorants, Mann-Whitney test $P = 0.0051$). Data are presented as box plots (25th and 75th percentiles) showing the mean in white. Whiskers represent the 10th and 90th percentiles. (**c**) Effect of CNO injection on the mean population correlation (normalized to its value in pre-CNO control condition and averaged across all pairs taken from 6 odors) in ChR2- and Gi-DREADD- expressing mice (Mann-Whitney test $P = 0.0055$). (**d**) CNO injection (2mg/kg; all groups injected) decreased learning performances in Gi-DREADD-expressing mice in comparison to ChR2- expressing mice (n = 9 mice in each group; repeated measures ANOVA $F = 6.32$ $P = 0.023$, post-hoc LSD test at least *$P < 0.045$). Odor pair used: AC/LI 60/40 vs. AC/LI 40/60 (gas mixes).